Bayesian inference of fog visibility from LiDAR point clouds and correlation with probabilities of detection

Karl Montalban, Christophe Reymann, Dinesh Atchuthan, Paul-Edouard Dupouy, Nicolas Rivière, Simon Lacroix

Bayesian inference of fog visibility from LiDAR point clouds and correlation with probabilities of detection

Karl Montalban[1,2,3], Christophe Reymann[1], Dinesh Atchuthan[1],
Paul-Edouard Dupouy[2], Nicolas Rivière[2] and Simon Lacroix[3]

Abstract—Degraded visual environments have strong impacts on the quality of LiDAR data. Experiments in artificial fog conditions show that noise points caused by water particles present various distance distributions which depend on visibility. This article introduces a mathematical framework based on Bayesian inference and Markov Chain Monte-Carlo sampling to infer optical visibility from point clouds. The visibility estimation is cast as a classification problem based on the identification of the distance distributions. Contrary to deep learning methods, our approach is model-based and focuses on the design of a full probabilistic framework, more comprehensible, which is critical for autonomous driving. Ultimately, the impact of the optical visibility on the probability of detection of standard targets is assessed, which can yield improvements on autonomous vehicles performances in adverse weather conditions.

I. INTRODUCTION

Autonomous Vehicles (AVs) rely on a variety of sensors, among which LiDAR (Light Detection and Ranging) sensors play a growing role. But Degraded Visual Environments (DVE) significantly impact LiDAR data, whatever the wavelengths used, the type of emission (beam steering, flash emission) and detection (single pixel or focal plane array, full waveform or single photon detection). In presence of fog or rain, the proximity between the laser wavelength and the water particle sizes causes interactions that degrade the overall quality of LiDAR data [1]. Scattering and absorption effects generate artifacts in the point clouds, non detections, reduces the signal to noise ratio and limits the maximum range of detection, which all obviously have significant consequences on the AVs' behavior.

Although weather events are complex (distribution of the droplets diameter, speed, density, etc.), common metrics exist to quantify them. For example, rainfall intensity is given in mm/h and fog opacity can be estimated as the optical visibility in *meters* (the International Civil Aviation Organization defines the visibility or meteorological optical range as "the greatest distance at which a black object of suitable dimensions, situated near the ground, can be seen and recognized when observed against a bright background" – see details in [2]).

[1]EasyMile, 21 Boulevard de la Marquette, 31000 Toulouse, France
[firstname.lastname]@easymile.com

[2]ONERA/DOTA, Université de Toulouse, 31055 Toulouse, France
[firstname.lastname]@onera.fr

[3]LAAS-CNRS, Université de Toulouse, CNRS, 7, Avenue du Colonel Roche, 31031 Toulouse, France
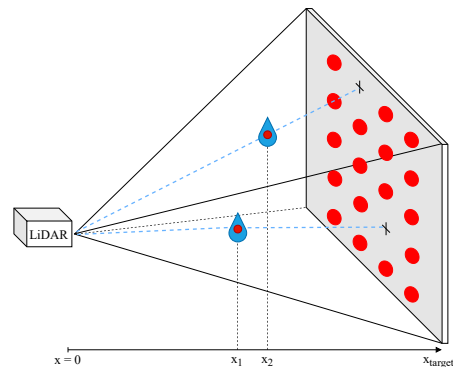[firstname.lastname]@laas.fr

Fig. 1. Schematic representation of the extraction of points inside a sensor to target frustum. Water particles generate artifacts and non-detections.

Be it for rain, snow, or fog, visibility is prone to rapid changes, and so its impact on the LiDAR data. Information on the weather conditions are essential to adapt data processing algorithms and improve the performances of AVs. Knowing the impact of weather conditions on the sensor probabilities of detection (POD), the input parameters of filtering algorithms can be adjusted according to the properties of rain, snow or fog [3], [4], [5], [6], [7].

Weather conditions assessment with LiDARs: Various work focus on the recovery of weather conditions with the use of automotive LiDARs. They consider the problem as a classification one, and most propose a statistical analysis of the impacts of the water particles. [8], [9], [10] estimate the nature of the weather conditions (clear, rain, fog, snow), using machine learning techniques (KNN, SVM with different feature vectors, or convolutional neural networks).

A probabilistic hierarchical Bayesian model is proposed in [11] to predict rainfall intensity. The model is trained using point cloud data acquired in artificial rain and a disdrometer to assess the rainfall ground truth. Artifacts caused by rain are used to train and test the model, which yields a measurement error of 2.89 mm/h, similar to the error of the disdrometer itself. The considered scene is free of obstacles (with the exception of the walls of the climatic chamber), and the whole point cloud is used, which results in a high number of artifact points. But the model may not be applicable in realistic scenes with a variety of structures of different reflectivity surrounding the sensor.

In fog conditions, Miclea et al. [12] propose methods to evaluate visibility in artificial conditions using the physical equations of light extinction in fog (Mie theory) and visual observations. In [13], [14], a machine learning approach focuses on LiDAR point clouds taken in artificial fog con-

ditions. A statistical analysis of the impacts of fog on range measurements is used to build a Gaussian process regression model. Given a certain visibility, the model predicts the range at which an object can be detected by the LiDAR.

Contribution and outline: This article focuses on the inference of optical visibility from automotive LiDAR point clouds in fog conditions. It proposes a method based on Bayesian estimation and Markov Chain Monte-Carlo (MCMC) sampling technique [15], [16]. We advocate a probabilistic approach yields a more controllable and comprehensible solution than a deep learning approach. This explicability is crucial to guarantee operational safety of an AV. The model is trained on point cloud data taken in artificial fog conditions, using a transmissiometer for the visibility ground truth. Distance distributions of echoes at close range for a specific LiDAR sensor are used. The Gamma distribution models the likelihood of fog echoes distances. The classification model is trained and tested for a series of visibility classes. Finally, the inferred visibility classes are used to assess the visibility impact on the POD of several standard targets.

The next section presents the experimental conditions in which data have been acquired. Section III introduces the inference model, and experimental results of visibility classification and POD estimations are presented in section IV.

II. EXPERIMENTAL SETUP

The LiDAR used for this study is the OUSTER OS1-128 spinning 3D-LiDAR [17]. It uses 865 *nm* wavelength vertical cavity surface emitting laser (VCSEL) and single-photon avalanche diode detectors (SPAD). Two columns of 128 emitters and detectors spinning around a vertical axis provide the 360° field-of-view (FOV) with 128 point layers. The minimum range of the sensor is around 0.25 *m* and a single echo can be returned for each laser shot.
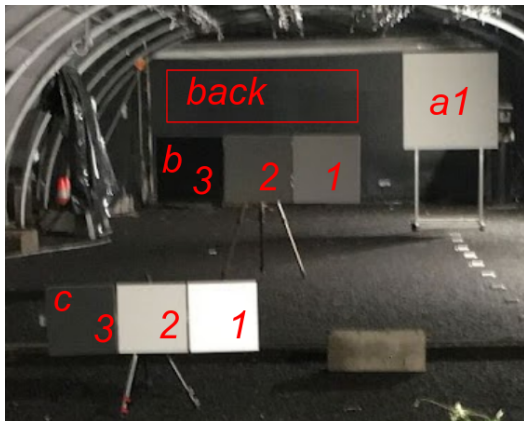

Fig. 2. Targets of interest inside the climatic chamber.

Data has been acquired in the CEREMA[1] climatic chamber in Clermont-Ferrand, France, in which artificial fog and rain conditions can be produced [18]. We focus on fog

conditions and the experiment is as follows : the climatic chamber is saturated with fog particles and point clouds are recorded as fog dissipates while visibility is being measured by a transmissiometer.

TABLE I
TARGETS PROPERTIES IN CLEAR CONDITIONS

Target	*back*	*a1*	*b1*	*b2*	*b3*	*c1*	*c2*	*c3*
Distance	29 *m*	23 *m*	17 *m*			11 *m*		
Surface	1.5 m^2	1 m^2	0.25 m^2			0.09 m^2		
# Points	109	86	45			35		

Different Lambertian targets of calibrated reflectance are located in the climatic chamber, as shown Fig. 2. Table I lists their characteristics with the number of returned data points in clear fog-less conditions. Fig. 1 illustrates the extraction process performed on the point clouds, where the frustum is defined by a target. In fog conditions, knowing a target size and position, all points that lie within the associated frustum at a distance closer than the target distance correspond to artifacts caused by water particles. This extraction process allows us to assess the POD of a target along with the associated noise generated by the sensor.

The *back* target is used to train and test the visibility inference model, and targets *a1*, *b1*, *b2*, *b3*, *c1*, *c2* and *c3* are considered to analyze the impacts of inferred visibility on the POD of standard targets at different distances and reflectivities. The *back* target is chosen because its properties (tab. I) give more frustum detections and thus more data for the inference model. Ideally, one would consider frustum points from a FOV free of target but it is not available in the considered experimental conditions and the *back* target is the best approximation available.

III. METHODOLOGY

We seek to infer the current optical visibility by using the distribution of echoes distances located in the frustum between the sensor and a target. We choose a Bayesian inference approach to assess in which class of visibility the sensor is being operated. A Monte-Carlo sampling technique is used to learn the parameters of Gamma distributions which best fit the distance distributions of echoes in each class of visibility. The model produces probabilities for each visibility class which offer means to assess the solution quality and could be extended with external and/or a priori knowledge. The next section explains why the Gamma distribution can be used as an appropriate sensor model. Then, the equations describing the Bayesian inference framework are detailed.

A. Gamma distribution

The Gamma distribution is introduced in the context of AVs sensors in [4] to model the distance repartition of echoes from LiDAR point clouds in snowfall conditions. Also under snow conditions, Michaud et al. [19] expose similar distance distributions of echoes, but suggest to use the Log-normal distribution to fit the distance histograms. They also state that the shapes of the distance distributions arise from the product between an "optical detection" function and

a "building shielding effect" because the sensors are located at a building window. Sata et al. [20] study the properties of light reflected from fog particles and objects captured by SPAD detectors in a LiDAR design. They showcase that the time profiles of fog and objects photon returns respectively have Gamma and Gaussian distributions. This allows them to extract real targets inside fog and reconstruct the 3D scene. Considering the application of laser pulses in fog conditions, the resulting signal on the LiDAR detector is a combination of the laser pulse shape, considered as Gaussian, an atmospheric extinction function, which can be modeled as a decreasing exponential function, and of the detector response. This yields a product similar to a Gaussian function restricted to the positive domain, and therefore with a longer decreasing tail. In the absence of a more refined model and according to the literature, both Gamma and Log-normal distributions seem valid candidates to model the distance distribution of fog echoes returned by a LiDAR.
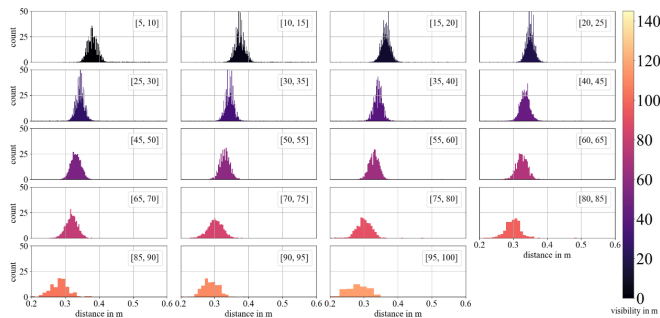

Fig. 3. Normalized distance histograms of frustum fog points detected with the *back* target for each visibility class from [5, 10] to [95, 100] by steps of 5*m*. Color refers to visibility in m.

Fig. 3 displays the distance histograms of the frustum points detected by the LiDAR for different fog visibility classes (more details in section IV) where colors reflect visibility values. Their shape convinced us to use the Gamma distribution to model this likelihood. The probability density function (PDF) of the Gamma likelihood of measuring a fog echo at range x, parametrized with shape γ and scale β, is defined by :

$$G(x) = \frac{1}{\Gamma(\gamma)\beta^\gamma} x^{\gamma-1} e^{-\frac{x}{\beta}} \quad (1)$$

with $\Gamma(\gamma)$ the Gamma function evaluated at γ.

B. Inference model

A LiDAR is aiming at a target and operating in fog conditions. At a given time, a set of echoes distances $E = \{e_1, e_2, ..., e_n\}$ from the sensor to target frustum containing noise points is received. Let $Y = \{(E_i, v_i)\}$ for $i \in [1, m]$, be the training dataset built from the experiments in artificial fog conditions. It consists of distances $E_i = \{e_1, e_2, ..., e_l\}_i$ and discrete optical visibilities v_i.
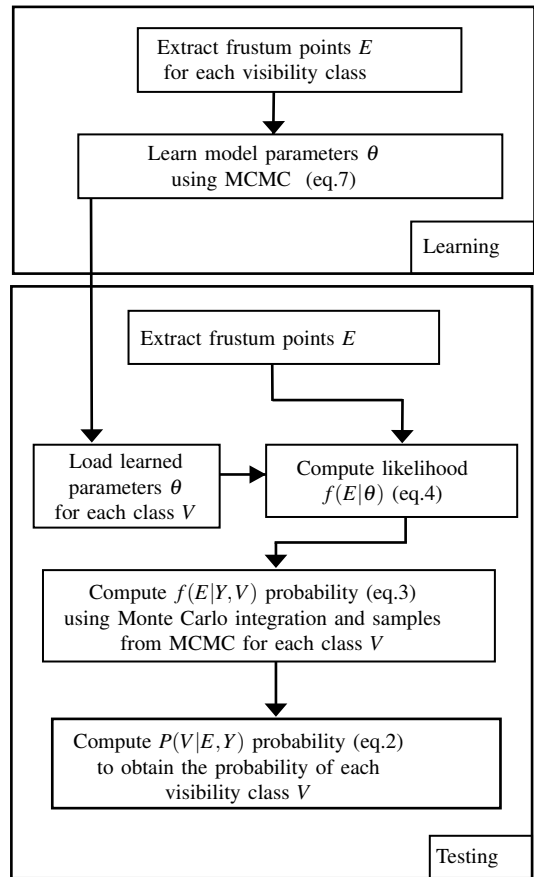

Fig. 4. Schematic diagram of the Bayesian inference framework.

The probability of having a visibility value v knowing a set E and the dataset Y is $P(v|E,Y)$. Using Bayes' theorem, we have:

$$P(v|E,Y) = \frac{f(E|Y,v).P(v|Y)}{\sum_{i=1}^{m} f(E|Y,v_i).P(v_i|Y)} \quad (2)$$

where $f(E|Y,v)$ is the likelihood of the continuous echoes distances E for a specific visibility v, and $P(v|Y)$ is the prior probability on the discrete visibility value, which is considered uniform.

Let θ be a pair of shape γ and scale β parameters which describes the Gamma likelihood distribution of our sensor model. We introduce θ as a hidden variable of the system, linking E to (Y,v) through marginalization over θ, $f(E|Y,v)$ becomes :

$$f(E|Y,v) = \int_\theta f(E|\theta)f(\theta|Y,v)d\theta \quad (3)$$

The density distribution $f(E|\theta)$ is the likelihood of the echoes given the parameters θ. The events of receiving echoes are independent, thus this likelihood is a product of probabilities following a Gamma distribution.

$$f(E|\theta) = \prod_{e \in E} G(e|\theta) \quad (4)$$

The continuous density $f(\theta|Y,v)$ represents the learned model parameters of the Gamma distributions generated by

the fog echoes observed at a given visibility v. Considering that the pairs (E_i, v_i) in Y are also independent, $f(\theta|Y, v)$ becomes

$$f(\theta|Y, v = v_i) = f(\theta|E_i, v = v_i) \tag{5}$$

This means that θ only depends on the part of the training dataset Y acquired at the specific visibility v. We use Bayes' theorem again to expose the likelihood of E_i knowing θ:

$$f(\theta|E_i, v_i) = \frac{f(E_i|\theta, v_i)P(\theta|v_i)}{\int_\theta f(E_i|\theta, v_i)P(\theta|v_i)d\theta} \tag{6}$$

Similarly to the PDF $f(E|\theta)$, $f(E_i|\theta, v_i)$ can be modelled by a Gamma distribution with independent events so that,

$$f(\theta|E_i, v_i) = \frac{\prod_{e \in E_i} G(e|\theta)P(\theta, v_i)}{\int_\theta \prod_{e \in E_i} G(e|\theta)P(\theta, v_i)d\theta} \tag{7}$$

Equation (7) can then be used directly to learn a model of θ for each visibility level.

During the inference phase, equation (2) is used to infer a probability for each visibility level using the learned models through (3). To best approximate $f(\theta|E_i, v_i)$ during the training phase, we sample it using a MCMC method and save the sampled representation of the distribution for each visibility level. When frustum echoes are received, these trained samples are used to compute the probabilities of each visibility level. Using the sampled representation of equation (3), $f(\theta|E_i, v_i)$, can easily be computed by Monte-Carlo integration. Fig.4 gives a schematic representation the total inference framework.

IV. EXPERIMENTAL RESULTS

A. Distance distribution of LiDAR echoes in fog conditions

The dataset used in this study is composed of time-stamped point clouds and visibility values. Fig. 5 shows the rise of visibility captured by the transmissiometer over time as fog dissipates in the chamber.
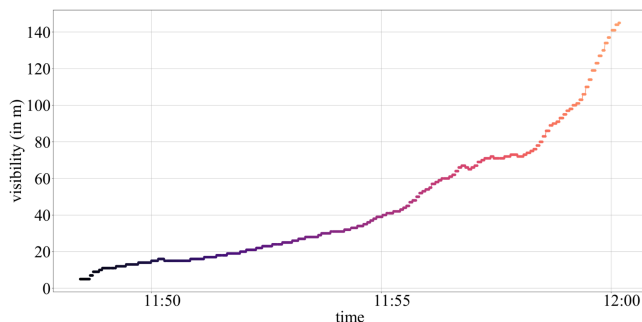
Fig. 5. Visibility over time measured by the transmissiometer during the fog dissipation.

On Fig. 6 the evolution of the POD of the *back* target (in circles) and frustum (in crosses) points is shown. These POD are calculated by dividing the number of points found in the scans with the average number of points n_{clear} found in clear conditions on the *back* target (see Table I).
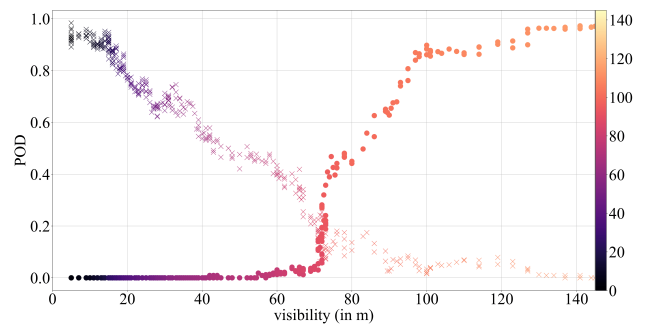
Fig. 6. Probability of detections of target (circles) and frustum (crosses) points over visibility, color refers to visibility. The sum of target and frustum PODs may not equal to 1 as some laser shots may not produce any echo.

As Ouster spinning LiDARs always shoot their laser beams with the same heading, n_{clear} is treated as the number of laser beams fired towards the target, considering that the sensor works in single return mode. Thus, this normalization is suitable for both frustum and target points. Frustum points are dominant when visibility is the lowest with almost 100% of detections. Their number decreases as fog dissipates while the number of points detected on the target increases. The visibility measurements range from 5 m (lower limit of the transmissiometer) to 145 m (no points in the frustum) with a precision of 1m. Finally, the dataset used for training and testing the inference model is composed of 3419 LiDAR scans, which amounts to a total of 239261 frustum points. Fig.3 shows that the majority of the frustum points are located around 0.3 m. Beyond 0.4 m, white noise can be observed in the data but it is negligible and does not impact our results. The vicinity of these points makes them usable for inference in realistic scenes because it is unlikely for solid targets to be located at such small distances in a classic urban AV scenario. One can see that as visibility increases, the number of frustum points decreases and they tend to get closer to the sensor. This evolution in distance may be due to unknown signal processing internal to the sensor.

B. Classification results

To evaluate our proposed model and for the sake of simplicity, we convert the inference problem to a classification one and use our model as a multi-class classifier. Instead of visibility values we infer visibility intervals, which we treat as discrete classes. The wideness of the visibility classes is constrained by our dataset, to ensure enough data is available to train the prior model on each class. During the inference, the inferred class is the most probable one. The dataset is split into a training set ($2/3$ of the scans) and a test set ($1/3$ of the scans). Fig. 6 indicates that the number of frustum points (in crosses) decreases with the dissipation of fog. When this number is too low, the data is insufficient to perform the test nor the training calculations. A threshold of 10 points is chosen and this sets a maximum value of visibility for the inference to 100 m. The inference is performed on 19 visibility classes set from 5 to 100 m by steps of 5 m. Classification results are shown on Fig. 9 as a confusion matrix. Each row corresponds to the classification result for a ground truth class, where results are normalized

by the number of tests for that class. The results show that the method is capable of inferring classes close to the ground truth. However the model results in a null probability to infer some classes. While this should be investigated, given the low amount of data available for this study and the inference of neighbouring classes in these worst cases, the proposed method still remains relevant.
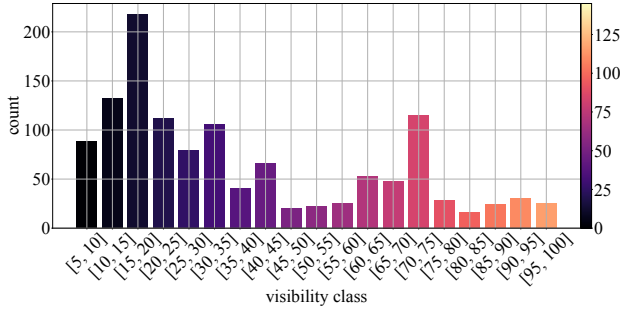

Fig. 7. Number of LiDAR scans used for the test phase for each visibility class.

Although converting the inference problem to a classification one and discarding the probabilistic information is bound to yield a degradation in performance, most of inferred classes are close to the ground truth class, without significant outliers. To more finely evaluate inference quality, we may compute a root mean squared error (RMSE) from the confusion matrix using the following equation:

$$RMSE_v = \frac{\sum_{i=1}^{N} (v_i - \hat{v}_i)^2}{N} s \qquad (8)$$

where v_i is the ground truth class number, $\hat{v}_i$ is the inferred class number, s is the visibility step of each class and N is the number of classes. Computed on the confusion matrix (fig.9), $RMSE_v = 6.3\,m$, which is barely above the 5 m discretization size.

The visibility and number of frustum points do not evolve constantly during the acquisition, as shown in figures 5 and 6. Therefore the number of LiDAR scans and thus the number of LiDAR points available for the classification differ for each class. Fig.7 shows the number of scans for each class available for the test phase. Results of the classification are mitigated by this non-uniformity in the dataset. Considering this non-uniformity, the 1 m precision of the transmissiometer and the 5 m range of our visibility classes, our model remains robust and shows relatively good performances. However, no conclusion can be made on its generalization capabilities, as training and testing is performed on data from one single climatic chamber.

C. Impact on the probability of detection of standard targets

In terms of AV's operability, visibility is less meaningful than the sensors' capacity of detection. Information about a sensor's POD can help to adapt the speed of an AV or parameters of perception algorithms. Using the influence of visibility over POD (shown in fig.6 for the *back* target), the inferred visibility classes can be used to indicate the resulting sensor's POD of a target.
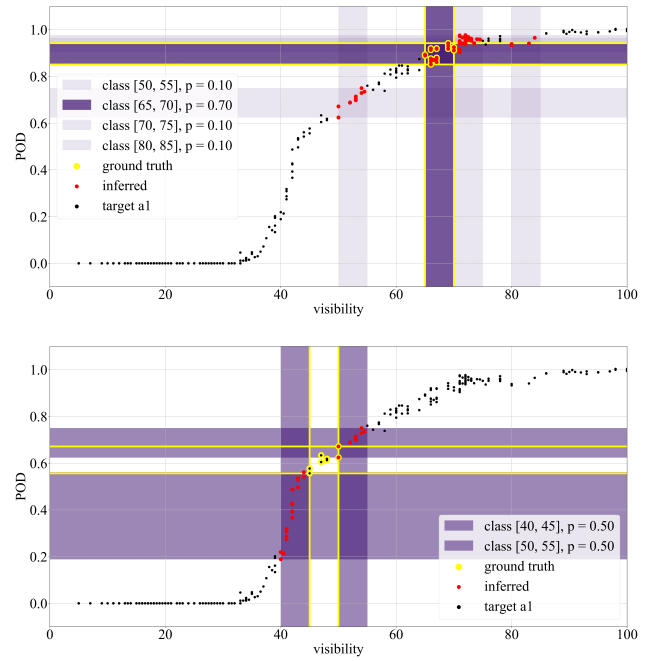

Fig. 8. Retrieval of $a1$ target POD from the inferred visibility classes and targeted classes $[65, 70]$ (top) and $[45, 50]$ (bottom). For a ground truth visibility class, the inferred classes are represented with vertical purple bands and the level of transparency shows the probability value of inference. Target POD values can then be extracted using the points inside the purple bands, highlighted in red. Yellow lines and points indicate the results drawn from the ground truth.

Fig.8 shows two examples of the impacts the inferred visibility classes have on the $a1$ target's POD where the targeted visibility classes are respectively $[65, 70]$ and $[45, 50]$. It illustrates that the 5 m size of visibility class can lead to high errors in the retrieval of POD for specific visibility classes. Especially for classes containing high variations in POD values, such as the $[40, 45]$ class for which the POD range from 0.2 to 0.6 and the class is inferred with probability $p = 0.5$ when targeting class $[45, 50]$.

Finally, the total classification results and different targets can be used to evaluate $RMSE_{POD}$ errors over the POD of targets at different distances and reflectivity values. It is calculated with the following equation :

$$RMSE_{POD} = \sum_{j=1}^{M} (POD_{gt,i} - min(POD_{inf,j}))^2 p_{inf,j} \qquad (9)$$

where M is the number of inferred classes and i the targeted class. $POD_{gt,i}$ is the average POD from ground truth, $POD_{inf,j}$ is the POD data points from the inferred classes, and $p_{inf,j}$ is the probability of each inferred class j. Fig.10 showcases the mean POD with associated $RMSE_{POD}$ from all visibility classes inferred during the test phase and two different target configurations. The top and bottom plots respectively show the corresponding values for the three available high reflectivity targets $a1$, $b1$ and $c1$ and for the three Lambertian targets $b1$, $b2$ and $b3$ located at 17 m. It should first be noted that errors are of the same order of magnitude for all targets. As expected, the slope of the POD curve strongly influences the resulting $RMSE_{POD}$ of each
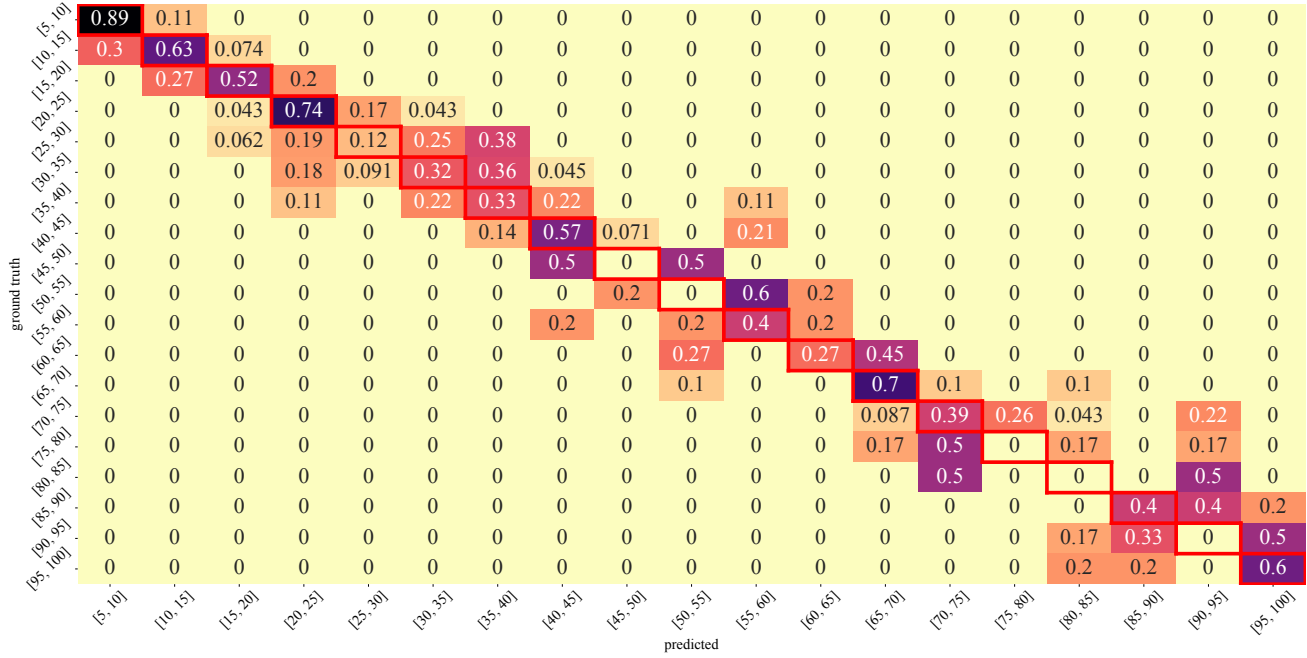
Fig. 9. Confusion Matrix from visibility classification using the *back* target in fog dissipation. Visibility classes range from [5, 10] to [95, 100] by steps of 5*m*.

target. Errors made on the POD are quite low when the POD slope is also low, and inversely higher $RMSE_{POD}$ values are seen when the POD increases. This is partly due to the 5 *m* step of our visibility classes: smaller classes would lead to higher precision of POD.
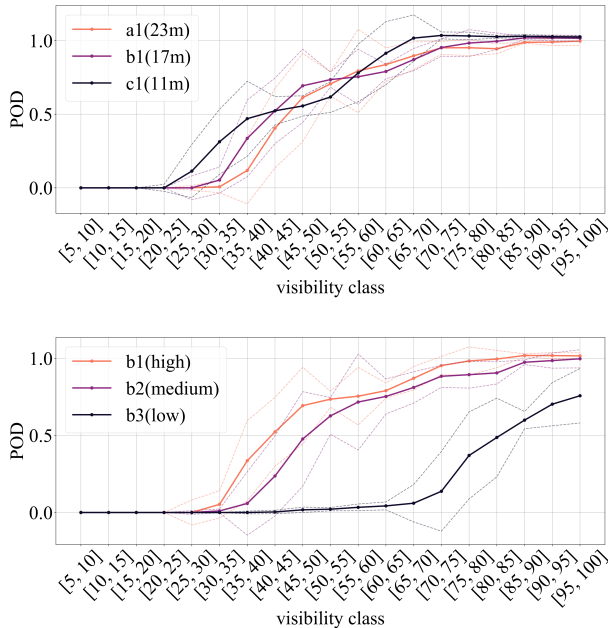

Fig. 10. Evolution of POD and corresponding $RMSE_{POD}$ for each visibility class and different targets. Top: result for three high reflectivity targets at different ranges. Bottom: results for three targets at the same distance but with different reflectivities.

V. CONCLUSION

Physical interactions between fog particles and laser beams shot by the Ouster OS1-128 LiDAR create identifiable distance distributions in the point clouds at close range. Trained on artificial conditions with a transmissiometer as ground truth, the presented Bayesian inference model is able to infer optical visibility from the identification of Gamma distance distributions. Inferred classes of visibility range from 5 to 100 meters by steps of 5 *m* and classification shows an RMSE error of 6.3 *m* over visibility. This result is satisfying considering the small size of the dataset, its non-homogeneity and the ground truth measurement errors from the transmissiometer. The method is generic and can be easily adapted to different classes of visibility to better match the user's needs. Resulting probabilities of detections are drawn from the visibility classification and the results can be used to improve the operability of AVs in classic urban scenarios. The enforced presence of a solid object in the FOV is a limitation of the climatic chamber. The presented model is trained on the OS1-128 LiDAR data. Its use with another LiDAR sensor requires a specific training due to different distance distributions results. Future work includes the expansion of the dataset since additional data from the same artificial conditions are expected to strengthen the accuracy of the model. Data from outdoor acquisitions are then needed to verify the reliability of the inference in real-world fog conditions. In operational outdoor conditions, a FOV free of target could be used with the same methodology. Additionally, the model can be completed by considering the amplitude of the distance distributions along with their shape, using Random Finite Sets (RFS) models. Finally, the classification of visibility and correlation with probabilities of detection using a probabilistic method could be used to comply with certification standards and reach higher Automotive Safety Integrity Level (ASIL).

REFERENCES

[1] R. Rasshofer, M. Spies, and H. Spies, "Influences of weather phenomena on automotive laser radar systems," *Advances in Radio Science*, vol. 9, 07 2011.

[2] I. C. A. Organization, *Meterological Service for International Air Navigation. Annex 3 to the Convention on International Civil Aviation. Part I Core SARPs. Part II Appendices and Attachments*. ICAO, 2010.

[3] N. Charron, S. Phillips, and S. L. Waslander, "De-noising of lidar point clouds corrupted by snowfall," in *2018 15th Conference on Computer and Robot Vision (CRV)*, 2018, pp. 254–261.

[4] S. Ronnback and A. Wernersson, "On filtering of laser range data in snowfall," in *2008 4th International IEEE Conference Intelligent Systems*, vol. 2. IEEE, 2008, pp. 17–33.

[5] Y. Duan, C. Yang, H. Chen, W. Yan, and H. Li, "Low-complexity point cloud denoising for lidar by pca-based dimension reduction," *Optics Communications*, vol. 482, p. 126567, 2021.

[6] J.-I. Park, J. Park, and K.-S. Kim, "Fast and accurate desnowing algorithm for lidar point clouds," *IEEE Access*, vol. 8, pp. 160 202–160 212, 2020.

[7] A. Kurup and J. Bos, "Dsor: A scalable statistical filter for removing falling snow from lidar point clouds in severe winter weather," *arXiv preprint arXiv:2109.07078*, 2021.

[8] R. Heinzler, P. Schindler, J. Seekircher, W. Ritter, and W. Stork, "Weather influence and classification with automotive lidar sensors," in *2019 IEEE Intelligent Vehicles Symposium (IV)*, 2019, pp. 1527–1534.

[9] J. R. Vargas Rivero, T. Gerbich, V. Teiluf, B. Buschardt, and J. Chen, "Weather classification using an automotive lidar sensor based on detections on asphalt and atmosphere," *Sensors*, vol. 20, no. 15, p. 4306, 2020.

[10] G. Sebastian, T. Vattem, L. Lukic, C. Bürgy, and T. Schumann, "Rangeweathernet for lidar-only weather and road condition classification," in *2021 IEEE Intelligent Vehicles Symposium (IV)*. IEEE, 2021, pp. 777–784.

[11] R. Karlsson, D. R. Wong, K. Kawabata, S. Thompson, and N. Sakai, "Probabilistic rainfall estimation from automotive lidar," *ArXiv*, vol. abs/2104.11467, 2021.

[12] R.-C. Miclea, C. Dughir, F. Alexa, F. Sandru, and I. Silea, "Laser and lidar in a system for visibility distance estimation in fog conditions," *Sensors*, vol. 20, no. 21, p. 6322, 2020.

[13] Y. Li, P. Duthon, M. Colomb, and J. Ibanez-Guzman, "What happens for a tof lidar in fog?" *IEEE Transactions on Intelligent Transportation Systems*, vol. 22, no. 11, pp. 6670–6681, 2021.

[14] T. Yang, Y. Li, Y. Ruichek, and Z. Yan, "Lanoising: A data-driven approach for 903nm tof lidar performance modeling under fog," in *2020 IEEE/RSJ International Conference on Intelligent Robots and Systems (IROS)*. IEEE, 2020, pp. 10 084–10 091.

[15] C. M. Bishop, *Pattern Recognition and Machine Learning*. Springer, 2007.

[16] D. Koller and N. Friedman, *Probabilistic graphical models: principles and techniques*. MIT press, 2009.

[17] https://ouster.com/resources/webinars/digital-vs-analog-lidar/.

[18] K. Montalban, C. Reymann, D. Atchuthan, P.-E. Dupouy, N. Riviere, and S. Lacroix, "A quantitative analysis of point clouds from automotive lidars exposed to artificial rain and fog," *Atmosphere*, vol. 12, no. 6, 2021. [Online]. Available: https://www.mdpi.com/2073-4433/12/6/738

[19] S. Michaud, J.-F. Lalonde, and P. Giguere, "Towards characterizing the behavior of lidars in snowy conditions," in *7th Workshop on Planning, Perception and Navigation for Intelligent Vehicles, IEEE/RSJ International Conference on Intelligent Robots and Systems (IROS)*, 2015.

[20] G. Satat, M. Tancik, and R. Raskar, "Towards photography through realistic fog," in *2018 IEEE International Conference on Computational Photography (ICCP)*, 2018, pp. 1–10.